Flux-Pinned Dynamics Model Parameterization and Sensitivity Study

Frances Zhu
Cornell University
452 Upson Hall
Ithaca, NY 14853
913-777-9595
Fz55@cornell.edu

Laura Jones-Wilson
Jet Propulsion Laboratory,
California Institute of Technology
4800 Oak Grove Dr.
Pasadena, CA 91109
Laura.L.Jones@jpl.nasa.gov

Mason Peck
Cornell University
455 Upson Hall
Ithaca, NY 14853
607-255-4023
Mp336@cornell.edu

Abstract— Flux-pinned interfaces for spacecraft are an action-at-a-distance technology that can maintain a passively stable equilibrium between two spacecraft in close-proximity using the physics of magnetic flux pinning. Although flux pinning dynamics have been studied from a material-science perspective and at an interface level, there is a need to better understand the sensitivities and implications of system-level designs on the flux-pinned interface dynamics, especially in designs with multiple magnets and superconductors. These interfaces have highly nonlinear, coupled dynamics that are influenced by physical parameters including but not limited to strength of magnetic field sources, field-cooled position, and superconductor geometry. This paper addresses that gap by codifying parametric terms into an improved dynamics model, which can then be used to simulate the interaction of a multiple-superconductor-multiple-magnet interface. A standard starting point for modeling flux pinning dynamics is Kordyuk's frozen image model, which defines a geometric mapping between magnetic field sources and their corresponding magnetic point source "images inside the volume of the superconductor." The frozen image model successfully approximates the characteristics of flux pinning dynamics, but could provide more precise position and orientation predictions with the addition of various physical parameter refinements. The sensitivity of the general flux-pinned dynamics model is studied by varying the physical parameters and simulating the systems level dynamics. A predictive dynamics model is crucial to the maturation of this technology so it can be utilized in spacecraft systems, and this work represents a critical step in the development of that model.

TABLE OF CONTENTS

1. INTRODUCTION

Flux-pinned interfaces (FPIs) leverage the dynamics of magnetic flux pinning to control the relative orientation and position of close-proximity spacecraft without mechanical contact. This unique set of traits makes FPIs a technology candidate for applications such as spacecraft capture and docking [1] [2], assembly of modular systems [3] [4], formation flying [5] [6] [7], kinematic mechanisms [8] [9], and station-keeping [10] [11]. However, for this technology to mature to the point of viability for a flight project, it is essential to develop a high-fidelity predictive dynamics model that can inform design trade and analyses. Available closed-form dynamics models of the interactions are valuable for their qualitative capturing of the basics of the interaction but are too coarse to serve as an effective guide for the design process. Thus, this work is an effort to develop the tools necessary to empirically determine modifications to the existing dynamics model so that it can better predict time and frequency responses for systems outfitted with an FPI.

2. BACKGROUND

Flux Pinning Magnetization Models

In a system of magnets and type II superconductors, two conventional methods of modeling magnetization behavior include the critical state model and the advanced frozen image model. Both models macroscopically represent changes in the superconductor embedded magnetic field as external field changes but express the magnetization differently. Bean's critical-state model expresses the internal magnetic field as a distribution of electron current vortices at the superconductor boundary [12]. Kordyuk's frozen image model geometrically maps a magnetic field source as a dipole into paramagnetic and diamagnetic image reflected across the superconductor boundary and moving virtually within the superconductor volume [13].

The two methods differ in complexity and scope of modeling a superconducting system. Bean's critical-state model superimposes a multitude of magnetization loops to represent a magnetic source. The critical-state model increases in accuracy and fidelity as the resolution of magnetization loops

is refined, but is also more numerically intensive [14]. Due to its numerical nature, the critical-state model is valid for an arbitrary superconductor geometry and magnetic field gradient. The computational intensity of the critical-state model may be restrictive for real-time applications and systems of many magnets and superconductors. Kordyuk's frozen image model generates two virtual magnetic moment dipoles for each independent magnet and superconductor interaction. Two closed-form analytical image representations drastically simplify the macroscopic behavior, especially for a system of multiple magnets and superconductors. The frozen image model is simple enough to simulate real time dynamics, which have natural modes as fast as hundreds of Hertz. For a system of M superconductors and N magnets, the frozen image model computes processes at an order of $\sigma(MN^2)$. The critical state model is not only compounding across every superconductor and magnet, but also across every mesh node P of each object, at an order of $\sigma(MP_M^2N^2P_N^4)$, an immense amount of computation. The frozen image model offers the simplicity of a closed-form solution to the dynamics, but in doing so, it makes many assumptions about the superconducting system which reduces the model's fidelity.

Frozen Image Model Derivation

Kordyuk's analytical model offers a six degree-of-freedom geometric mapping and a consequent dynamic model. We will follow Kordyuk's derivation of the frozen image model and test the assumptions laid out in his derivation. Once a type II superconductor is cooled below the critical temperature, Kordyuk's model calls for the creation of two images, called the frozen image and the mobile image. For a magnet field-cooled with initial position r_{FC} and magnetic moment m_{FC}, the frozen image position is r_f and magnetic moment m_f, shown in **Error! Reference source not found.**. he frozen image remains static while the mobile image moves with its magnetic field source, reflecting in both position and orientation across the superconductor surface. ρ_m is the distance between the corresponding mobile image and magnet, ρ_f the frozen image to magnet. The following equations form the basis of the frozen image model, maintaining the external magnetic field gradient in the presence of disturbances.
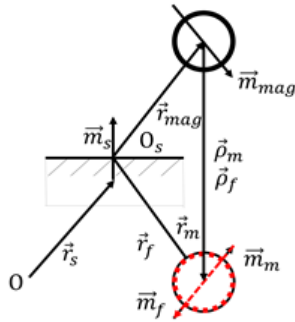

Figure 1: Geometric relationship between the equilibrium,

$$H_z(\rho - r_{FC}, m_{FC}) = H_z(\rho - r_f, -m_f) \qquad (1)$$

$$H_z(\rho - r_{mag}, m_{mag}) + H_z(\rho - r_m, -m_m) = 0 \qquad (2)$$

$$H_{im}(r) = H(r - r_f, m_f) + H(r - r_m, -m_m) \qquad (3)$$

$$B(r) = H(\rho - r_{FC}, m_{FC}) + H_{im}(r) \qquad (4)$$

The external magnetic field H_z of the permanent magnet is equivalent to the internal magnetic field of the frozen image within the superconductor upon the process of field-cooling a frozen image into the superconductor, shown in Eq. (1). The magnetic field contribution H_z from both the magnet and mobile image add to no net magnetic field disturbance, mathematically represented by Eq. (2). The sum of the frozen image, from Eq. (1), and from the diamagnetic image, from Eq. (2), is defined as the image field H_{im}, Eq. (3). Kordyuk explicitly derives the magnetic field outside the superconductor as the sum of the permanent magnet field and image fields $B(r)$, given by Eq. (4) [15]. These equations, specifically (1) and (2), form the basis for dynamics derivations and carry a series of fundamental assumptions that are discussed below.

The frozen image magnetic moment dipole is defined by the field-cooled magnet's position and strength, in which some important geometric parameters are not included. Eq. (1) assumes the frozen image dipole is of the same strength as the magnet dipole field-cooled to the superconductor, a one to one mapping. Instead of representing the source magnet as a dipole of varying strength, an analogous representation of the magnetization behavior is the percentage of total magnetic flux from the source dipole penetrating the volume of the superconductor. The relative size of the magnet and superconductor scales the percentage of flux captured in the superconductor [16]. The embedded magnetic field is agnostic to the location of the field-cooled magnet, which is valid for an infinite plane, but invalid for a superconductor of finite surface [17]. The magnet's location relative to the superconductor surface also determines the strength of the frozen image. The mobile image is dictated by many of the same pitfalls and more.

In an ideal superconductor, the mobile image exactly compensates for a change in magnetic field, the source magnet. The ideal superconductor expels all disturbances but for a real superconductor, the magnetic field may penetrate through the superconductor boundary, making the right side of Eq. (2) nonzero. Much like the frozen image, the mobile image is defined by the source magnet's position and orientation and are affected by the same geometric parameters: relative geometry, the magnet source's relative position, and orientation. The source magnet may also generate a mobile image of differing strength upon approach and exit but does not permanently change the system, elastic

magnetic hysteresis [18] [19] [20].The source magnet may permanently change the embedded magnetic field after field-cooling in a process called flux creep, plastic magnetic hysteresis [21] [22] [23]. Outside the fundamental physics, the explicit geometric expressions also carry underlying assumptions.

Equations (5) to (10), below, formalize both images' magnetic moment dipole as a geometric function of position and orientation of both the source magnet and superconductor, depicted geometrically in **Error! Reference ource not found.**. Subscript m and f correspond to the mobile image and frozen image, respectively. $\hat{m}_s$ is the unit direction normal to the surface of the superconductor. ρ_f and ρ_m is the distance from the image to the source magnet, where r_f and r_m is the location of the image and O_s is an arbitrary point on the superconductor surface. This formulation assumes that the strength, orientation, and location of the frozen image map one to one with the field-cooled magnet and remain fixed. Many of the same assumptions from Eq. (1) apply to Eq. (5) and Eq. (8). In this set of equations, there lies an explicit relationship between the superconductor orientation and location and image definition. By using $\hat{m}_s$ to represent the direction normal to the superconductor surface in Eq. (5) and (6), Kordyuk assumes that the superconductor plane is flat, without manufacturer defects, and of single domain [24] [25]. On an infinite superconductor plane, O_s serves as a reference point that is arbitrarily placed. This reference point must be strategically placed on a finite surface of the superconductor due to the reference point's effect on representing total flux captured in the superconductor volume. The full geometric definition of the images is then used in the governing equations of motion.

$$m_f = \left(2\hat{m}_s\,\hat{m}_s^T - \underline{1}\right)m_{mag} \tag{5}$$

$$\rho_f = r_{FC} - r_f \tag{6}$$

$$r_f = r_{FC} - 2\left((r_{FC} - O_s)\cdot\hat{m}_s\right)\hat{m}_s \tag{7}$$

$$m_m = \left(\underline{1} - 2\hat{m}_s\,\hat{m}_s^T\right)m_{mag} \tag{8}$$

$$\rho_m = r_{mag} - r_m \tag{9}$$

$$r_m = r_{mag} - 2\left((r_{mag} - O_s)\cdot\hat{m}_s\right)\hat{m}_s \tag{10}$$

Governing Equations of Motion

To create a dynamics model incorporating flux-pinned interactions, the frozen image model is combined with Villani/Landecker's analytic solutions for force and torque between two magnet dipoles [26] [27]. The force and torque

of a magnetic dipole m_b acting on another magnetic dipole m_a at distance ρ, are given by Eq. (11) and (12).

$$F_{ab} = \frac{3\mu_0 m_a m_b}{4\pi\rho^4}\Big((\hat{\rho}\times\hat{m}_a)\times\hat{m}_b + (\hat{\rho}\times\hat{m}_b)\times\hat{m}_a - 2\hat{\rho}(\hat{m}_a\cdot\hat{m}_b) +$$
$$5\hat{\rho}\big((\hat{\rho}\times\hat{m}_a)\cdot(\hat{\rho}\times\hat{m}_b)\big)\Big) \tag{11}$$

$$\tau_{ab} = \frac{\mu_0 m_a m_b}{4\pi\rho^3}\big(3(\hat{m}_a\cdot\hat{\rho})(\hat{m}_b\times\hat{\rho}) + (\hat{m}_a\times\hat{m}_b)\big) \tag{12}$$

For a rigid body with M static superconductors interacting with a rigid body of N magnets, the total force and torque acting on the body is the sum of every source magnet interaction across every image, across all superconductors. The underlying force equation reduces to an arbitrary source magnet i interacting with both images of magnet j across superconductor k's surface, given by Eq. (13). The total force on each source magnet i is the sum of all forces from each magnet j's images across all superconductors k, given by Eq. (14). The total force acting through the center of mass on the magnetic rigid body is the sum of all forces across every source magnet, given by Eq. (15). The moment on source magnet i is the sum of moments across all images produced by magnet j across all superconductors k and a resultant torque from a force on source magnet i across the respective moment arm, given by Eq. (16). Analogous to the body force equation, the moment on the rigid body is the sum of moments across all source magnets i, given by Eq. (17). Any modifications on the general interaction between a source magnet and image is compounded across M superconductors, $2N$ magnet images, and N source magnets, a resultant magnification of $2MN^2$.

$$F_{ijk} = F_f + F_m \tag{13}$$

$$F_i = \sum_{j=1}^{N}\sum_{k=1}^{M}F_{ijk} = \sum_{j=1}^{N}\sum_{k=1}^{M}\left(\left(F_f + F_m\right)_k\right)_j \tag{14}$$

$$F_{COM} = \sum_{j=1}^{N}F_i = \sum_{i=1}^{N}\sum_{j=1}^{N}\sum_{k=1}^{M}\left(\left(\left(F_f + F_m\right)_k\right)_j\right)_i \tag{15}$$

$$\tau_i = \sum_{j=1}^{N}\sum_{k=1}^{M}\left(\left(\tau_f + \tau_m\right)_k\right)_j + \rho_i \times F_i \tag{16}$$

$$\tau_{COM} = \sum_{i=1}^{N}\sum_{j=1}^{N}\sum_{k=1}^{M}\left(\left(\left(\tau_{frozen} + \tau_{mobile}\right)_k\right)_j\right)_i + \sum_{i=1}^{M}\rho_i \times F_i \tag{17}$$

The dynamic states, position, velocity, attitude, and angular velocity, are then propagated by a set of generic 6 degree-of-freedom rigid body dynamic equations. Newton's linear moment balance yields position and velocity state propagation, given by Eq. (18) and (19). The angular momentum balance yields angular velocity and quaternion state propagation, given by Eq. (20) to (22). The linear

damping term in Eq. (18) and (20) accounts for air drag and eddy current effects that dissipate the oscillatory motion. By updating the state of the rigid body, the individual states of the source magnets are then propagated and updated for the frozen image model, closing the loop of the system dynamics model.

$$\Sigma \boldsymbol{F} = M\ddot{\boldsymbol{r}} + C\dot{\boldsymbol{r}} \tag{18}$$

$$\ddot{\boldsymbol{r}} = M^{-1}(\Sigma \boldsymbol{F} - C\dot{\boldsymbol{r}}) \tag{19}$$

$$\Sigma^{N}\boldsymbol{\tau} = I \cdot \frac{^{B}d\boldsymbol{\omega}}{dt} + \boldsymbol{\omega}_{B/N} \times (I \cdot \boldsymbol{\omega}_{B/N}) + C\boldsymbol{\omega}_{B/N} \tag{20}$$

$$\dot{\boldsymbol{\omega}}_{B/N} = I^{-1} \cdot (\Sigma^{N}\boldsymbol{\tau} - \boldsymbol{\omega}_{B/N} \times (I \cdot \boldsymbol{\omega}_{B/N}) - C\boldsymbol{\omega}_{B/N}) \tag{21}$$

$$\dot{q} = \frac{1}{2}q \otimes \omega \tag{22}$$

## 3. FROZEN IMAGE MODEL IN APPLICATION

In this section, we'll discuss the assumptions from the frozen image model with more depth, supporting literature that extends the basic model, and a mathematical formulation to account for these effects in the dynamics model. Kordyuk assumes properties about the superconducting system that are outside the context of the equations. After field-cooling a magnet to a superconductor, the imprinted magnetic field varies in strength due to temperature, material properties, and geometry of the superconductor. Although not explicitly stated, Kordyuk assumes binary temperature activation, in which past a certain critical temperature, the material is fully superconducting. Chiang and Jiang have instead found that levitation force between a magnet and superconductor is first noticeable past the critical temperature and continuously stronger as the superconductor is brought to lower temperatures [28] [29]. Superconducting properties also do not activate unless magnetic field penetrating the superconducting boundary crosses a threshold of magnetic field strength, which changes with temperature as well [30] [31]. The threshold magnetic field strength differs in various superconducting materials and in orientation with respect to the planes of the material structure. Superconductors not only have a minimum magnetic field threshold, but a maximum magnetic field saturation boundary, related to the critical current density of the material [32].The interactions are also highly anisotropic, depending on the grain-alignment of the superconductor structure and magnetic field [33] [34] [35]. At a fundamental level, this model assumes that the magnets are perfect dipoles, much like spherical magnets, which does not accommodate an arbitrary magnetic field source. The model also assumes that the superconductor disc is an infinite plane, not true of real finite dimensioned superconductor discs. There are implicit assumptions embedded within the structure of the frozen image model equations. These assumptions affect the entire system and are ubiquitous to all magnet and superconductor interactions. Outside the geometry of the magnet, the refinements are all related to uncertainty or higher order effects derived from the superconductor behavior in the context of flux pinning: environment temperature, material properties, superconductor geometry [36].

Temperature

Temperature affects flux pinning interactions in two ways: maximum levitation force and elastic hysteresis. Unlike Kordyuk's inherent assumption of binary activation in superconductors, observations suggest the superconducting phenomenon is continuously activated. Chiang and Jiang both found that the colder the superconductor, the more levitation force and less hysteresis are emphasized in the force curves [28] [29]. Although both investigators studied YBCO samples, the relationship between levitation force and temperature disagree, as seen in *Figure 2*. The discrepancy may lie in the samples each investigator chose. Chiang used superconductor samples on the scale of a couple millimeters with a magnet much larger than the superconductor (roughly four times the surface area), whereas Jiang used a superconductor 30 mm in diameter and a magnet slightly smaller than the superconductor. For the small superconductor samples, the hysteresis gaps are very evident and temperature variation does not taper off, but seemingly extends linearly. For the large superconductor samples, the temperature variation tends to taper off as the superconductor reaches 40 K and hysteresis affects the force path negligibly. A general trend may be drawn, that colder temperatures offer stronger interactions, but a precise scaling factor cannot be extrapolated from these two studies.

Levitation Force Dependence on Temperature (Chiang)
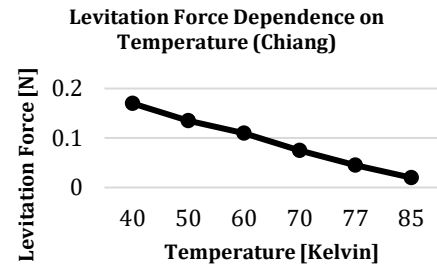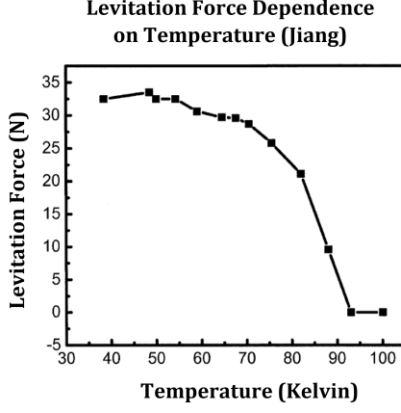
Figure 2: Comparison of Chiang and Jiang's results on levitation force and temperature relationship [28] [29].

To incorporate the variation of temperature into the dynamics model, the formulation for the mobile and frozen image magnetic moment dipoles are modified with a scaling factor $c_t(T|T_{ref})$, given by Eq. (23) and (24). T is the temperature in which the superconductor operates and T_{ref} is the reference temperature in which the levitation force was measured, separated by the condition given operator '|'. c_t is greater than 1 when $T < T_{ref}$, less than 1 when $T > T_{ref}$, and equal to 1 when $T = T_{ref}$. $c_t(T|T_{ref})$ can be found through interpolation or extrapolation of the empirical dataset provided by Chiang or Jiang [28] [29], but due to disagreement, the most accurate method to determine the scaling factor is to measure the temperature variation for specific magnet and superconductor used in the specific application.

$$\boldsymbol{m_m} = c_t(T|T_{ref})\left(\underline{1} - 2\hat{\boldsymbol{m}}_s\hat{\boldsymbol{m}}_s^T\right)(\boldsymbol{m_{mag}}) \qquad (23)$$

$$\boldsymbol{m_f} = c_t(T|T_{ref})\left(2\hat{\boldsymbol{m}}_s\hat{\boldsymbol{m}}_s^T - \underline{1}\right)(\boldsymbol{m_{FC}}) \qquad (24)$$

Material Properties

The material properties of the superconductor vary the behavior of the flux-pinned interaction immensely, ranging from the elemental composition, manufacturing process, and crystalline structure. The elemental composition affects the critical temperature at which the superconductor is superconducting, its lower and upper critical field, and the critical current density [30]. Yttrium Barium Copper Oxide (YBCO) has been studied extensively due to its heritage, high critical temperature, and high critical magnetic fields. In addition, YBCO superconductor discs exhibit flux pinning above liquid nitrogen's boiling temperature, which is inexpensive and accessible. YBCO also has no known material safety hazards [37]. To model the dynamics, the lower critical magnetic field bounds affect the interaction continuity, the higher critical magnetic field bounds affect the strength of the interaction, and hysteresis affects the

predictability of the system.

An intrinsic property of a superconductor is the elemental composition. Important energy parameters, like critical temperature and thermodynamic critical field, are defined by the material composition. At a microscopic level, the material affects the surface impedance at low fields, acting through intermediate-state tunneling, in which a lower threshold of critical field must be surpassed to give rise to any electromagnetic interaction. The weak tunnel coupling emphasizes anisotropy in different crystalline structures, such as copper, bismuth, or thallium planes [30]. For a YBCO sample structure (copper oxide planes) of specific temperature and geometry, the lower critical field is 0.1 T perpendicular to the plane and 0.02 T parallel to the plane [31]. The macroscopic geometry of the superconductor, such as surface area and volume shape, also play an important role in critical field thresholds and caution must be used when implementing these thresholds.

The lower critical field threshold effect is modeled as a discontinuous magnetic regime transitioning from no current excitation to current excitation. Treating the magnet as a singular dipole, the interaction is considered binary. Treating the magnet as a flux field, the interaction is better encapsulated as a continuous scaling of the dipole. B_a, the applied field, is the magnetic field penetrating the superconductor at its boundary. B_a is a function of the strength and orientation of the magnet dipole, the position w.r.t the superconductor surface, and the superconductor surface normal. If B_a is above the minimum critical threshold B_c, there exists a virtual magnetic image that interacts with the source magnet, given by Eq. (25) and (26).

$if\ \boldsymbol{B_a}(\boldsymbol{m_{FC}}, \boldsymbol{r_{FC}}, \hat{\boldsymbol{m}}_s) > \boldsymbol{B_c},$

$$then\ \boldsymbol{m_f} = \left(2\hat{\boldsymbol{m}}_s\hat{\boldsymbol{m}}_s^T - \underline{1}\right)\boldsymbol{m_{FC}} \qquad (25)$$

$if\ \boldsymbol{B_a}(\boldsymbol{m_{mag}}, \boldsymbol{r_{mag}}, \hat{\boldsymbol{m}}_s) > \boldsymbol{B_c},$

$$then\ \boldsymbol{m_m} = \left(\underline{1} - 2\hat{\boldsymbol{m}}_s\hat{\boldsymbol{m}}_s^T\right)\boldsymbol{m_{mag}} \qquad (26)$$

Manufacturing Process

Manufacturing processes define intrinsic properties of the superconductor. The internal structure and external geometry of the superconductor affect the strength and hysteretic behavior of the flux pinning physics. A bulk superconductor may be made in different ways, ranging from compressing grains into a mold or inducing melt textured growth of a single crystal in an oven.

Regardless of the manufacturing method, every superconductor has defects in its composition: surface smoothness, cracks, and impurities between copper planes [30]. Chan [38] fabricated superconducting samples with YBCO grains of various sizes and epoxy without aligning the

5

grains to investigate the effects on critical current density, levitation force, and hysteresis. The larger grained samples had a lower current density, larger maximum levitation force, and larger gap in the hysteresis curve. Similarly, Yang [24] sliced a large YBCO sample into smaller components to investigate the effect of different grain sizes on levitation force, while retaining the same grain orientation. The smaller components, when reassembled to resemble the original disc, did not provide the same amount of levitation force. The force linearly decreased as a function of number of cuts/parts. Yang [25] explores the specific consequences of cracks in the superconductor sample, showing that the larger the crack, the less levitation force the superconductor provided.

To maximize the levitation force offered by the superconductor, the optimal fabrication process is to produce a single domain superconductor sample. After the raw sample is grown, the sample may be cut in different geometries with intended surface area aligned along the grain. The largest measured levitation force occurs when the magnetic vector field is perpendicular to the copper planes, with a monotonically reduction of levitation force as the magnetic field becomes parallel with the copper planes [35] [33] [34]. The hysteresis gap is also observed to be largest when the copper planes are perpendicular to the applied field. The levitation force may be scaled as a function of relative alignment between the superconductor surface and magnetic moment dipole pole axis. Equation (27) characterizes this degradation, assuming the copper planes are parallel to the cut superconductor surface and the angle is zero when the moment dipole is aligned with the superconductor surface normal [35]. F is the resultant force, a value scaled down by a function of angle between the dipole and superconductor normal. The maximum levitation force F_0 measured at $\theta = 0°$, and the minimum levitation force F_{90} measured at $\theta = 90°$.

$$F = c_g(\theta)F_0 \tag{27}$$

$$c_g(\theta) = \cos^2\theta + \frac{F_{90}}{F_0}\sin^2\theta \tag{28}$$

The maximum levitation force reveals the strength and depth of the potential well of the magnetic system, but the shape of the potential is still left uncharacterized. The simplest dynamics model includes no hysteresis or negligible hysteresis, seen in very cold temperatures while flux-pinned [29]. If that is not the case, the levitation force paths vary in degrees of elastic hysteresis and inelastic or plastic hysteresis, which both affect equilibrium position and orientation.

Hysteresis

Hysteresis stems from elastic instabilities in the flux-line lattice that dissipate energy [21]. At a microscopic level, the flux line changes to a different energy state and is dissipated through tiny eddy currents in the current vortices. Due to the hysteresis that occurs during relative magnet-superconductor movement, the system can be brought to a continuous range

of stable equilibria positions and orientations [18]. For the recoverable or elastic hysteresis curves, Zhang [19] and Yang [20] have proposed modifications to the frozen image model by including a vertical and horizontal movement image that even accounts for saturation within the superconducting material. The addition of the two images accounts for the hysteresis gap but must be scaled by empirical data collected from the specific system of interest. Some hysteresis is not recoverable and plastic deformation in the internal magnetic field permanently changes the dynamic behavior of the system [21] [22] [23].

Geometric and Spatial Relationship

Extrinsic factors, such as geometry and spatial relationship, affect the way the source magnet flux penetrates the superconductor geometry, which then modifies the stiffness of the interaction. For a spherical superconductor, the geometric mapping from the source magnet to either image is different than for a flat surface superconductor [39]. Superconducting samples with the largest surface area and thickness offered the most levitation force. Thickness did not increase levitation force linearly but diminished in rate of influence [40]. By varying the relative size of the magnet and superconductor, the optimal magnet size is slightly smaller than the size of the superconductor, in which an increase in magnet diameter starts to reduce the stiffness of the flux-pinned interaction [16]. The magnetic field shape of the source magnet affects the levitation force profiles, leading to stiffer interactions in which the gradient of the magnetic field changed drastically, like corners or sharp edges [41]. These higher order effects are not accounted for in a dipole representation and the magnetic moment dipole equation must be modified for the magnet of interest.

The spatial relationship between the magnet and superconductor influences the flux penetration within the superconductor, related to the minimum critical field. Kordyuk assumes an infinite plane superconductor, but for practical purposes, no infinite geometries exist. As the source magnet moves farther from the center of the superconductor, the amount of flux penetrating the volume of the superconductor decreases, and thus the stiffness of the interaction also decreases [17]. Even when the magnet is field-cooled directly above the center of the superconductor, the frozen image strength is only 64% of the frozen image model anticipated strength. The strength of the images is scaled by distance from the center of the superconductor, given by Eq. (29) and (30). r_l, defined in Eq. (31), expresses the absolute distance from the center of the superconductor parallel to the surface of the superconductor and c_D, defined by Eq. (32), is a linear approximation of the degradation of strength as the magnet moves off the surface of the superconductor. c_D is found empirically where c_{max} is the portion of field captured in which the magnet is center above the superconductor and c_d is the reduction of field as a function of lateral distance r_l. Since the distance from the center of the superconductor is an important parameter in the

flux-pinned system, Kordyuk's formulation of the distance vectors in Eq. (7) and (10) are modified to no longer use an arbitrary point as the reference origin O_s but to reference the center of the superconductor.

$$m_m = \left(\underline{1} - 2\hat{m}_s \hat{m}_s^T\right)\left(c_D(r_{mag})m_{mag}\right) \tag{29}$$

$$m_f = \left(2\hat{m}_s \hat{m}_s^T - \underline{1}\right)\left(c_D(r_{FC})m_{FC}\right) \tag{30}$$

$$r_l = |r - (r \cdot \hat{m}_s)\hat{m}_s| \tag{31}$$

$$c_D \cong c_{max} - c_d r_l \tag{32}$$

Of the discussed properties and parameters, we will investigate the sensitivity of force and torque due to small discrepancies in knowledge or control of these parameters.

4. PARAMETERIZATION OF FLUX-PINNED INTERFACES

Physical Parameters Optimizing Performance

To design for real-world applications, there are design considerations at the systems level that can maximize stiffness in a flux-pinned interface. At a component level, the material properties of a superconductor are the dominant driving factors in the operations and capabilities of flux-pinned interactions. The other half of the interface, the magnet, matters in strength, size, and geometry. At a higher level, other considerations include the relative size and location of the magnet and superconductor. These physical parameters are controllable parameters during system design that optimize for stiffness, but do not contribute to the accuracy/fidelity of the dynamics model.

The superconductor produces the flux pinning phenomena and its attributes determine the operating range and capabilities of the interface. The most inherent characteristic of a superconductor is its material, and specifically in the context of flux pinning, the critical current density. There are many different materials used throughout the century since the discovery of superconducting materials, including Niobium, Cuprate, and Magnesium based compositions [32]. YBCO material exhibits strong pinning forces in moderate fields with a critical temperature above that of liquid nitrogen. Due to its accessibility, YBCO bulk superconductors garner academic interest and are actively studied. Other materials have higher critical current densities but are also require further cooling due to the lower critical temperatures. YBCO superconductors offer stiff joints for nanosatellite sized spacecraft while reducing the cooling power needed to activate flux pinning physics.

The superconductor bulk formation and fabrication impacts the stiffness of flux pinning physics within material bounds. Grown from a single crystal, a single domain superconductor

yields larger levitation forces and exhibit less hysteresis than a granular, epoxy-bonded superconductor, as discussed previously. In the context of integrating superconductors on a spacecraft, any cracks or imperfections in the boundary of the superconductor reduce the efficacy of the joint so the superconductor disc should be protected from impact. Grain alignment can be adjusted to maximize stiffness in a chosen direction, in which case the magnetic moment dipole aligns with the superconductor surface normal. The superconductor geometry and surface depend on the quality of cut and polish during manufacture.

When sizing the magnet and superconductor, the relative geometry and relative position of the magnet and superconductor determine the strength of the interaction. The flux-pinned interface is optimally stiff when both the diameter of the magnet and the superconductor are similar. Superconductor and magnet size are both bound by manufacturing capabilities, in which superconductor size is more limiting. Although larger superconductor and magnet combinations increase the flux penetrating the superconducting volume, the strength of the interaction does not scale with mass. In determining field-cooled orientation, aligning the magnetic moment dipole perpendicular to the superconductor surface, assuming the grain runs parallel to the surface, achieves the stiffest interaction. Field-cooled position depends on lateral and normal separation distance, in which lateral movement is motion parallel to the superconductor plane and normal separation distance is movement perpendicular to the superconductor plane. In designing for field-cooled separation distance, adjusting this separation is a trade between stiffness and collision mitigation. Stiffness in a system with a dipole magnet pinned with the dipole perpendicular to the superconductor surface, when measured along that perpendicular axis is proportional to the field-cooled distance to the 4th power. The closer distance also reduces the clearance between two spacecraft, which could make collisions more likely. A larger field-cooled distance decreases the stiffness but offers more clearance for a compliant arrest to occur. After the above parameters are optimized for performance, the following parameters are studied for model fidelity.

Physical Parameters Affecting Model Fidelity

To inform system level design on dynamics, different physical parameters are studied to evaluate the most dominant characteristics of the flux-pinned system. The dynamics model formulation is explicitly defined, but the physical parameters of the system are rarely exactly known. The important adjustable physical parameters are field-cooled rotation and position, magnet strength, and temperature coefficient, given by Eq. (33), described in the following paragraph. There are some physical characteristics that are inherent to the system and should be optimized outside the context of dynamic modeling, such as the superconductor grain alignment, surface smoothness, and material composition. The state of interest is the spacecraft's

position [x y z], velocity [$v_x v_y v_z$], acceleration, quaternion [$q_x q_y q_z q_s$], and angular velocity [$\omega_x \omega_y \omega_z$], given by Eq. (34), which are ultimately propagated by force and torque on the system. Dynamic properties of the system include stiffness, natural frequencies and modes, and potential energy.

$$\boldsymbol{p} = \left[\begin{array}{ccccc} \theta_{FC} & r_{FC} & z_{FC} & B_0 & c_{temp} \end{array} \right]^{\mathrm{T}} \tag{33}$$

$$\boldsymbol{x} = \left[\begin{array}{ccccccccccccc} x & y & z & v_x & v_y & v_z & q_x & q_y & q_z & q_s & \omega_x & \omega_y & \omega_z \end{array} \right]^{\mathrm{T}} \tag{34}$$

The parameters are integrated into the dynamics model by injecting them into frozen image model mapping and state equations. θ_{FC} is the angular displacement from the ideal field-cooled attitude and [$r_{FC} z_{FC}$] is the position displacement from the ideal field-cooled position, which causes a discrepancy in knowledge of superconductor location and orientation. [$\theta_{FC} r_{FC} z_{FC}$] affect the geometric mapping from source magnet to images, given by Eq. (5) to Eq. (10), and consequently the equilibrium position and orientation of the spacecraft. B_0 is the surface strength of the source magnet, which forms the magnetic moment dipole of the source magnet and the consequential image mapping. c_{temp} is the scalar coefficient that adjusts the strength of the images depending on the superconductor's temperature, given by Eq. (23) and (24).

These parameters are studied in the context of a single magnet and single superconductor system, then a multiple magnet and multiple superconductor system to emphasize the compounding effect and coupled nonlinear dynamics of certain parameters. The parameters operate under different length scales and to avoid unit specific sensitivity analysis, a related numerical parameter is offered with parameters perturbed by one percent.

5. SENSITIVITY STUDY OF FLUX-PINNED INTERFACES

Single Magnet and Single Superconductor System

A common pairing of magnet and superconductors for studying flux pinning dynamics involve Neodymium, NdFeB, permanent magnets and Yttrium Barium Copper Oxide, YBCO, bulk superconductors. All literature referenced in this paper is specific to YBCO material composition, and when relevant, NdFeB magnets. The magnet used in this study is a NdFeB, N42 grade, 0.75 in diameter spherical magnet of 8815 Gauss manufacturer specified maximum surface strength. The superconductor disc used in this study is a CAN melt textured $YBa_2Cu_3O_{7-x}$, single domain, 56 mm diameter 16 mm thick cylindrical superconductor disc [42]. The magnet is field-cooled 2.55 cm above the center of the superconductor with the pole aligned with the superconductor surface normal. The direction convention for studying the single magnet and single superconductor (SMSS) system shown in *Figure 3*.
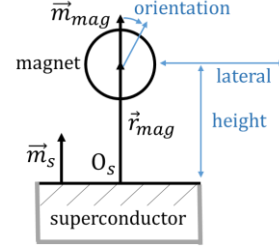

Figure 3: Direction convention for SMSS system.

SMSS Variation of Physical Parameters

To study meaningful variations of physical parameters, relevant parameters are offered to reference for scale. A summary of the physical parameters, reference parameter, numerical value of reference parameter, and numerical value of physical parameter perturbation is shown in *Table 1*. The misalignment of the magnet during field-cooling could be up to half the span of full reorientation due to symmetry, from and angle of zero to $\frac{\pi}{2}$. The field-cooled position radial displacement is with respect to the diameter of the superconductor, from zero to 28 mm. The field-cooled position height displacement is with respect to a chosen arbitrary field-cooling height 25.5 mm, from the center of the 19.1 mm diameter magnet to the center of the superconductor, from 9.5 to 41.5 mm. The magnetic field strength of the source magnet is with respect to the manufacturer specified surface field strength, from no strength (zero Gauss) to double the strength (17630 Gauss). Due to dissidence in current literature, temperature variation does not have an accurate model that relates temperature and levitation force. Instead, the temperature variation will be captured as a coefficient with respect to 1, from no flux pinning effect (zero) to double the effect (two).

Table 1: Summary of Physical Parameters with Relevant Reference Parameters for SMSS system.

Parameter to Vary	Relevant Parameter	Span of Relevant Parameter	Span of Variance
θ_{FC}	Pole to pole orientation	180 deg	[0 to 90] deg
r_{FC}	Diameter of superconductor	56 mm	[0 to 28] mm
z_{FC}	Separation distance/height	25.5 mm	[9.5 41.5] mm
B_0	Magnet surface field strength	8815 G	[0 17630] Gauss
c_{temp}	Temperature coefficient	1	[0 2]

We will investigate the dynamic response of the system as a result of perturbing these physical parameters. Appropriate metrics to characterize the performance of a flux-pinned interface include stiffness, depth of potential well, natural frequencies, magnitude of force and torque. The stiffness is the resistance of motion away from equilibrium position or

attitude. The potential energy is the energetic capability of the interface to capture a dynamic body and defines the sphere of influence across which the interface acts. Although natural frequency is directly related to stiffness, associating a realistic mass to a stiff joint yields physical intuition to system design. Magnitude of attractive force is a common metric to compare other physical phenomena acting on spacecraft. The sensitivity is represented as a series of plots across the entire span of each physical parameter with each dynamic response variable normalized to the reference response.

SMSS Sensitivity Results

By linearly varying the physical parameters across the entire span in *Table 1*, a relationship can be drawn from the magnet's dynamic response and the physical parameters. The following plots are separated by physical parameter, but each plot overlays the lateral stiffness, normal stiffness, rotational stiffness, potential energy, and force normalized to the reference response from the system described in *SMSS Physical System.* Noise stems from calculations perturbing the magnet state within machine precision error. When the physical parameter is equivalent to the reference value, the dynamic response is equivalent to the reference response and the normalized reference response is always 1, with reference responses given in *Table 2*. Any normalized values below 1 imply that the reference dynamic model overestimates the actual system's dynamic response, and vice versa for normalized values above 1. Due to the nonlinear behavior of flux-pinned dynamics, some physical parameter variation is amplified despite minimal perturbation. Lateral displacement is the only parameter in which a 1% variation results in less than 1% variation in the consequent dynamic response. When varying the most sensitive physical parameter, field-cooled height, the normal stiffness of the flux-pinned interface changed by over 10%, shown in *Figure 4*.

**Table 2: Reference Physical Parameters and Reference Dynamic Response Parameters for SMSS system.**

Reference Physical Parameter	Physical Parameter Numerical Value	Reference Dynamic Response Parameter	Dynamic Response Numerical Value
θ_{FC}	0 degrees	k_{lat}	29 N/m
r_{FC}	0 m	k_z	58 N/m
z_{FC}	0.016 m	k_{rot}	0.65 Nm/rad
B_0	8815 Gauss	U	-0.0109 J
c_{temp}	1	F	1.29 N
		ω_{lat}	32.7 rad/sec
		ω_{height}	46.5 rad/sec
		ω_{rot}	4.9 rad/sec

The system accumulates error, from least sensitive to most sensitive in field-cooled lateral displacement, field-cooled orientation, temperature, magnetic field strength, and field-cooled height. All dynamic response parameters decrease

linearly with increasing lateral displacement, with the scalar drawn from experiments measuring magnetic field within a YBCO superconductor disk, shown in *Figure 5*. Varying the field-cooled orientation from perfectly aligned to perfectly misaligned orientation shows monotonically degradation in every dynamic response except for rotational stiffness, which restored past 45 degrees, shown in *Figure 6*. The lateral stiffness was least affected and rotational stiffness was the most affected by orientation perturbation. Normal stiffness, potential energy, and attractive force were similarly degraded by orientation. All dynamic response parameters increase linearly with increasing temperature coefficient, shown in *Figure 7*. The linear relationships, temperature and lateral displacement, only affect the images, not the source magnet. All dynamic response parameters increase quadratically with increasing magnetic field strength, not linearly due to magnetic field strength affecting both the source magnet and image strength, shown in *Figure 8*. Field-cooled height affects all dynamic response parameters drastically, inversely proportional with r^4, shown in *Figure 9*.
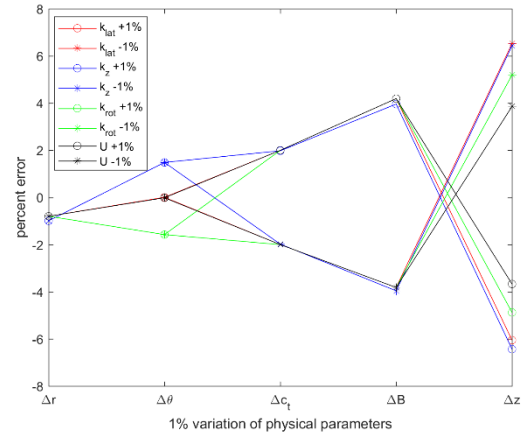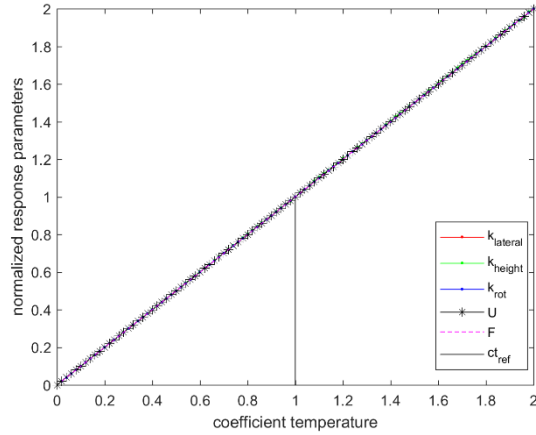

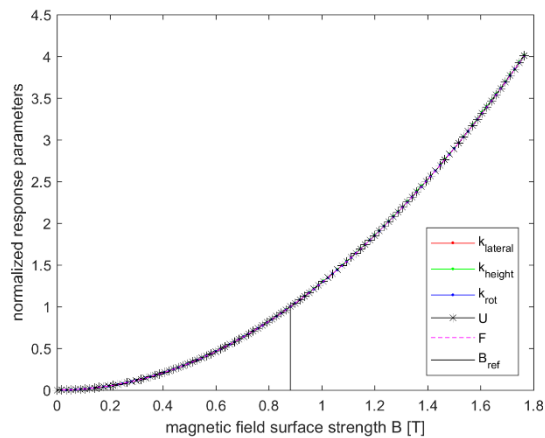**Figure 4: Percent error in dynamic response from 1% variation of physical parameters.**
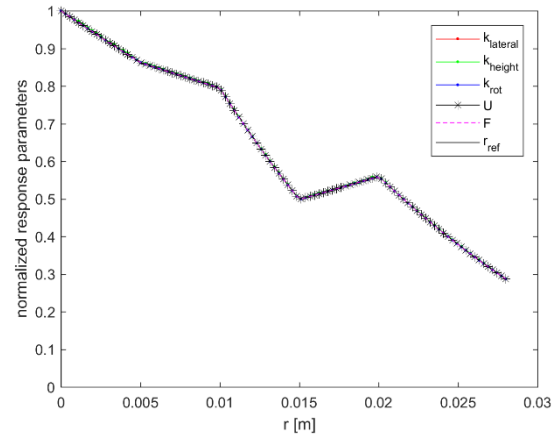
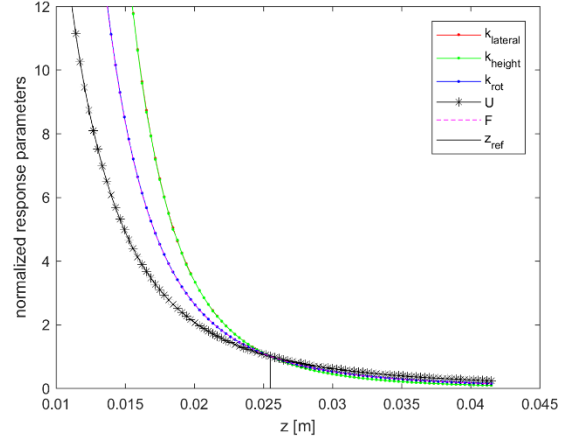**Figure 5: Dynamic response from field-cooled lateral displacement variation.**
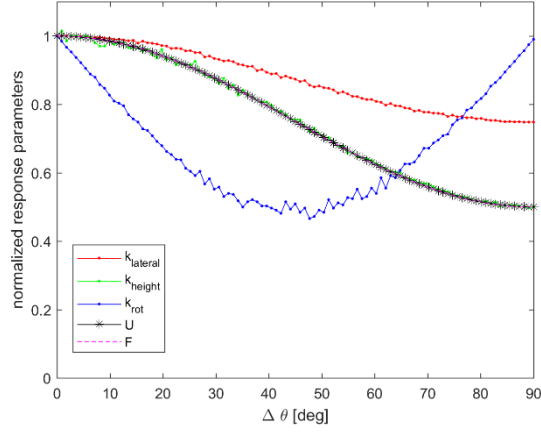
Figure 6: Dynamic response from field-cooled orientation variation.

**Figure 7: Dynamic response from coefficient of temperature variation.**

**Figure 8: Dynamic response from field-cooled magnetic field strength variation.**

Figure 9: Dynamic response from field-cooled height displacement variation.

Multiple Magnet and Multiple Superconductor System

The multiple magnet and multiple superconductor flux-pinned interface uses the same components and physical parameters described in the *SMSS Physical System* section but involves three superconductors and twelve magnets. In a case studying two spacecraft for a docking application, we define the magnetic spacecraft with a mass of 2.1 kg, 20.3 diameter sphere, as the orbiting satellite and the superconducting spacecraft as the spacecraft orbiter. The magnets are arranged in an icosahedron geometry, in which all magnets are pointing radially outward and equidistant from each neighboring magnet. The superconductors on the orbiter are placed so that any trio of the orbiting satellite's magnets are 2.55 cm radially inward in equilibrium position and pointed along the radial direction. This interface has been tested on a series of testbeds to study docking and capture dynamics, shown in Figure 10 [1]. Using the same dynamic response parameters, lateral, normal, and rotational directions must be defined analogously to the single magnet and single superconductor system, also shown in Figure 11.
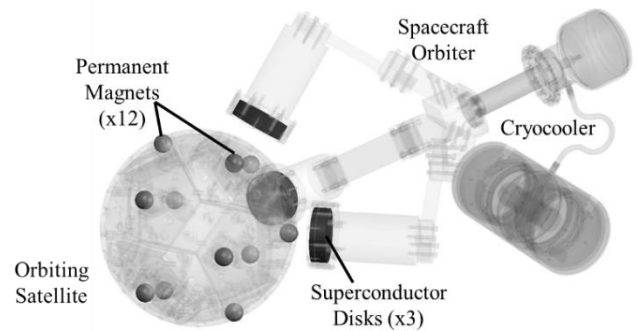
Figure 10: Multiple magnet and multiple superconductor flux-pinned interface of docking interface concept.
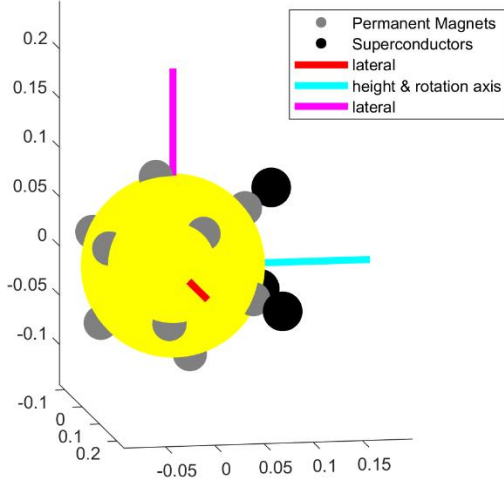
Figure 11: Direction convention for MMMS system.

MMMS Variation of Physical Parameters

Although the physical parameter symbols are analogous to the SMSS system, $\theta_{FC}, r_{FC}, z_{FC}$ represent slightly different physical parameters relating to the spacecraft, not an individual magnet. θ_{FC} is the angular displacement between two equilibria rotated about the center of the superconductors. As the spacecraft rotates about this axis, the magnets move off the superconductor surface at 16.5 deg. The lateral separation distance, r_{FC}, between the orbiting satellite and the orbiter spans from equilibrium position to physical interference between the two spacecraft bodies, symmetric in either direction. The lateral displacement never allows the magnet to move off the surface area of the superconductor because the two spacecraft surfaces interfere before the magnet moves too far in the lateral direction. The normal separation distance, magnetic field strength, and temperature coefficient cover the same spans. *Table 3* lists all parameters and the corresponding span of variance.

Table 3: Summary of Physical Parameters with Relevant Reference Parameters for MMMS system.

Parameter to Vary	Relevant Parameter	Numerical Value of Relevant Parameter	Span of Variance
θ_{FC}	Angular displacement between spacecraft EQ orientation	16.5 deg	[0 16.5] deg
r_{FC}	Lateral separation distance	8.5 mm	[0 8.5] mm
z_{FC}	Normal separation distance	25.5 mm	[-16 16] mm
B_0	Magnet surface field strength	8815 G	[0 17630] Gauss
c_{temp}	Temperature coefficient	1	[0 2]

MMMS Sensitivity Results

By linearly varying the physical parameters across the entire span in *Table 3*, a relationship can be drawn from the spacecraft's dynamic response and the physical parameters. The reference responses given in Table 4. Unlike the SMSS system, the MMMS rotational and translational degrees of freedom are coupled due to the source magnet and superconductor orientations spanning $\mathbb{R}^3$. The MMMS system is stiffer than the SMSS system in the translational degrees of freedom, but less stiff in the rotation. The baseline rotational stiffness is very low and any modifications to the system, like translational perturbation, transfers stiffness in translation to stiffness in rotation. Any perturbation in the system is amplified in the dynamic response to different degrees, shown in *Figure 12*. The most sensitive dynamic response is rotational stiffness. The physical parameter causing the most drastic change in a single dynamic response parameter is field-cooled orientation, but the change in the other dynamic responses are minimal. The physical parameter that affected the most distributed change across the entire system is field-cooled height.
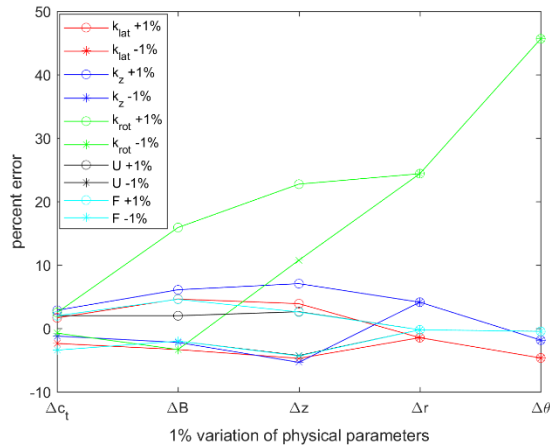
Table 4: Reference Physical Parameters and Reference Dynamic Response Parameters for MMMS system.

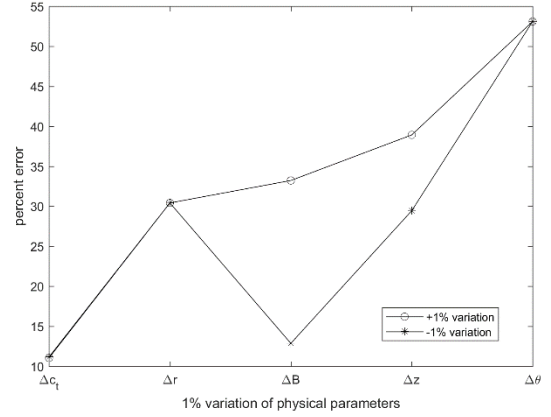| Reference Physical Parameter	Physical Parameter Numerical Value	Reference Dynamic Response Parameter	Dynamic Response Numerical Value
θ_{FC}	0 degrees	k_{lat}	65 N/m
r_{FC}	0 m	k_z	89 N/m
z_{FC}	0.016 m	k_{rot}	0.304 Nm/rad
B_0	8815 Gauss	U	0.0497 J
c_{temp}	1	F	1.8137 N
		ω_{lat}	5.57 rad/sec
		ω_{height}	6.53 rad/sec
		ω_{rot}	0.38 rad/sec

The system manifests the most error in any single dynamic response, from least sensitive to most sensitive, in temperature, magnetic field strength, field-cooled height, field-cooled lateral displacement, and field-cooled orientation, shown in *Figure 12*. The system accumulates the most error in any all dynamic responses, from least sensitive to most sensitive, in temperature, field-cooled lateral displacement, magnetic field strength, field-cooled height, and field-cooled orientation, shown in *Figure 13*. Temperature and magnetic field vary the MMMS system in the same way that they did in the SMSS system because these

parameters are agnostic to specific geometries. Temperature and magnetic field affect all magnet-superconductor interactions equally. The other physical parameters require a specific geometry context to explain the change in dynamic response.

The geometry specific parameters include field-cooled lateral displacement, height, and orientation. The lateral displacement, symmetric in the negative and positive direction, shifts one magnet closer to the corresponding superconductor surface in its normal direction, oppositely true for another magnet superconductor pair, and slides the last magnet laterally across the corresponding superconductor surface. Although the interaction between the laterally shifted and more separated magnet-superconductor pair is weaker, the closer magnet-superconductor more than compensates for the other reductions by increasing strength with r^3, increasing normal and lateral stiffness. Rotational stiffness depends on the lateral stiffness of individual magnet superconductor pairs, and scales less than an r^3 interaction. The field-cooled height for the spacecraft shifts every magnet superconductor pair equally, in a combination of normal and lateral direction with respect to each superconductor surface. The spacecraft dynamic responses are predictably stronger as the orbiting spacecraft is field-cooled closer to the orbiter. The MMMS system does not behave as dramatically to height variation as the SMSS system because the individual magnets also move in the lateral direction along the superconductor surface, reducing the amount of flux penetrating each superconductor. At the reference field-cooled orientation, each magnet moment dipole and superconductor surface normal pair is aligned, but as the field-cooled orientation gets larger, the magnetic moment dipoles and superconductor surface normal direction vectors are further misaligned, causing the reduction in lateral and height stiffness. The magnetic moment dipoles are closer aligned to the superconductor surface tangent, contributing to rotational stiffness, but with further angular displacement, the magnet is farther from the superconductor center in both lateral and normal distance.
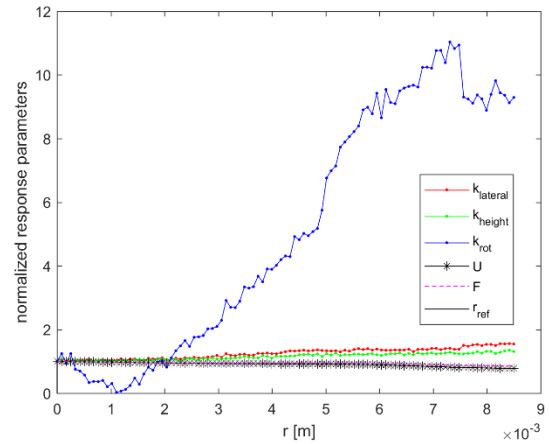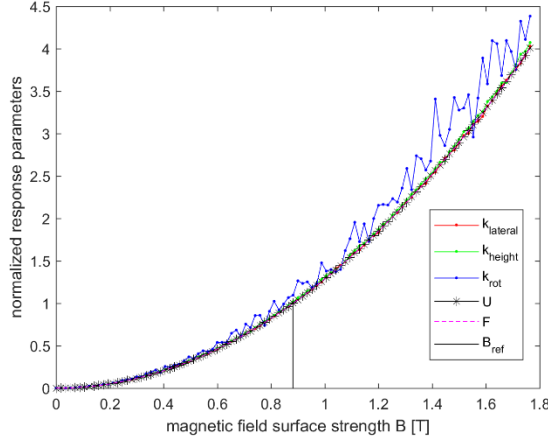

Figure 13: Accumulated percent error in dynamic response from 1% variation in each physical parameter.
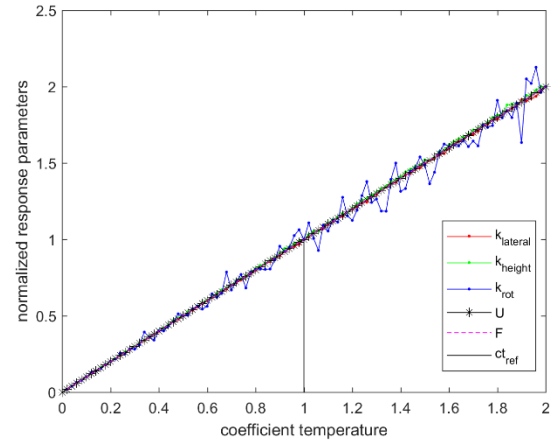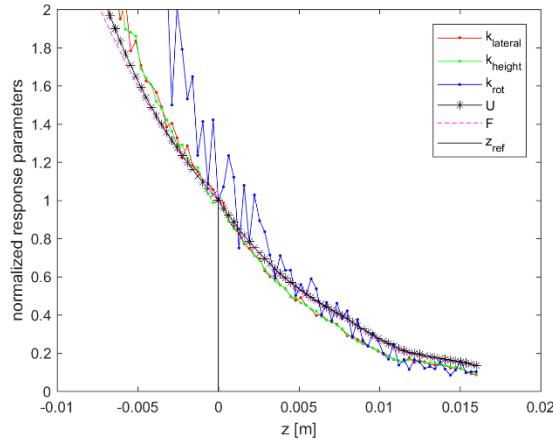

Figure 14: Dynamic response of system due to temperature coefficient variation.
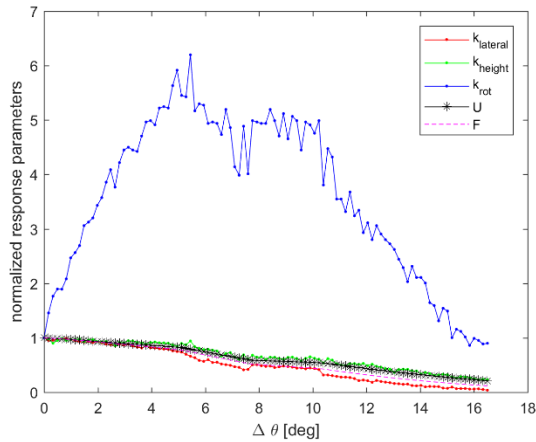

Figure 15: Dynamic response of system due to lateral displacement variation.

Figure 12: Percent error in dynamic response from 1% variation in each physical parameter.

12

Figure 16: Dynamic response of system due to magnetic field strength variation.

Figure 17: Dynamic response of system due to height variation.

Figure 18: Dynamic response of system due to field-cooled angle displacement variation.

6. CONCLUSIONS

In this paper, many modifications are suggested to refine Kordyuk's frozen image model. These modifications are based upon empirical data from that offer an explanation for discrepancies between ideal and physical system. The refinements are expressed in analytical form and injected into a dynamics model simulating flux-pinned interface dynamics. Two systems are described, based on commercially available components, to form a baseline dynamic response for single magnet single superconductor system and multiple magnet multiple superconductor system. Sensitivity studies are performed on each system to probe the effect of different physical parameters on the dynamic response of the system.

From the sensitivity study, system-level design considerations may be formed to target less error or emphasize certain dynamic responses. Some parameters are not geometry specific, like temperature and magnetic field strength, but all field-cooled parameters are geometry specific. In general, the field-cooled separation distance affects the system performance most significantly. When designing, integrating, or validating the specifications of a physical system, trade-offs are made weighing different dynamic characteristics, which are adjusted with knowledge of the consequences from each physical parameter. Outside control of system design, this sensitivity study informs technologists observing flux-pinning dynamics of potential sources and magnitudes of error from each physical parameter. In developing flux-pinned technology, this paper demonstrates the need to measure or control certain parameters with more precision to guarantee predictable dynamics below certain error bounds.

REFERENCES

[1] F. Zhu, L. Jones-Wilson and M. Peck, "A concept for capturing and docking spacecraft with flux-pinned interfaces," in *67th International Astronautical Congress*, Guadalajara, Mexico, 2016.

[2] L. Jones and M. Peck, "Stability and control of a flux-pinned docking interface for spacecraft," in *AIAA Guidance, Navigation, and Control Conference*, Toronto, 2010.

[3] J. Shoer and M. Peck, "Flux-Pinned Interfaces for the Assembly, Manipulation, and Reconfiguration of

Modular Space Systems," *The Journal of the Astronautical Sciences ,* vol. 57, no. 3, pp. 667-688, 2009.

[4] J. Shoer and M. Peck, "Simulation of multibody spacecraft reconfiguration through sequential dynamic equilibria," in *AIAA Guidance, Navigation, and Control Conference*, Toronto, 2010.

[5] J. Gersh and M. Peck, "Architecting the Very-Large-Aperture Flux-Pinned Space Telescope: A Scalable, Modular Optical Array with High Agility and Passively Stable Orbital Dynamics," in *AAS/AIAA Astrodynamics Specialist Conference*, Honolulu, Hawaii, 2008.

[6] L. Jones and M. Peck, "Prospects and Challenges of Particulate Solar Sail Propulsion," in *AIAA/AAS Astrodynamics Specialist Conference and Exhibit*, Honolulu, Hawaii, 2008.

[7] M. Norman and M. Peck, "Simplified Model of a Flux-Pinned Spacecraft Formation," *Journal of guidance, control, and dynamics,* vol. 33, no. 3, pp. 814-823, 2010.

[8] W. Wilson, J. Shoer and M. Peck, "Demonstration of a Magnetic Locking Flux-Pinned Revolute Joint for Use on CubeSat-Standard Spacecraft," in *AIAA Guidance, Navigation, and Control Conference*, Chicago, IL, 2009.

[9] J. Shoer and M. Peck, "Reconfigurable Spacecraft as Kinematic Mechanisms Based on Flux-Pinning Interactions," *Journal of Spacecraft and Rockets ,* vol. 46, no. 2, pp. 466-469, 2009.

[10] J. Shoer and e. al., "Microgravity Demonstrations of Flux Pinning for Station-Keeping and Reconfiguration of CubeSat-Sized Spacecraft," *Journal of Spacecraft and Rockets,* vol. 47, no. 6, pp. 1066-1069, 2010.

[11] M. Norman and M. Peck, "Stationkeeping of a Flux-Pinned Satellite Network," *Journal of guidance, control, and dynamics,* vol. 33, no. 5, pp. 1683-1695, 2010.

[12] A. Sanchez and C. Navau, "Vertical force, magnetic stiffness and damping for levitating type-II superconductors," *Physica C: Superconductivity,* vol. 268, no. 1-2, pp. 46-52, 1996.

[13] A. Kordyuk, "Magnetic Levitation for Hard Superconductors," *Journal of Applied Physics,* vol. 83, no. 1, pp. 610-612, 1998.

[14] A. Sanchez and C. Navau, "Critical current density from magnetiztion loops of finite high-Tc superconductors," *Superconductor Science and Technology,* vol. 14, no. 7, p. 444, 2001.

[15] J. L. Perez-Diaz and J. C. Garcia-Prada, "Interpretation of the method of images in estimating superconducting levitation," *Physica C: Superconductivity,* vol. 467, no. 1, pp. 141-144, 2007.

[16] H. Teshima, M. Sawamura, M. Morita and M. Tsuchimoto, "Levitation forces of a single-grained Y-Ba-Cu-O bulk superconductor of 48 mm in diameter," *Cryogenics,* vol. 37, no. 9, pp. 505-509, 1997.

[17] F. Zhu, M. Peck and L. Jones-Wilson, "Reduced Embedded Magnetic Field in Type II Superconductor of Finite Dimension," *in preparation.*

[18] C. Navau and e. al., "Equilibrium positions due to different cooling processes in superconducting levitation systems," *Superconductor Science and Technology,* vol. 17, no. 7, p. 828, 2004.

[19] X.-P. Zhang, Y.-H. Zhou and J. Zhou, "Modeling of symmetrical levitation force under different field cooling processes," *Physic C: Superconductivity,* vol. 468, no. 5, pp. 401-404, 2008.

[20] Y. Yang and X. Zheng, "Method for solution of the interaction between superconductor and permanent magnet," *Journal of Applied Physics,* vol. 101, no. 11, p. 113922, 2007.

[21] E. H. Brandt, "Friction in levitated superconductors," *Applied Physics Letters,* vol. 53, no. 16, pp. 1554-1556, 1988.

[22] E. H. Brandt, "Rigid levitation and suspension of high-temperature superconductors by magnets," *Americn Journal of Physics,* vol. 58, no. 1, pp. 43-49, 1990.

[23] X.-Y. Zhang, Y.-H. Zhou and J. Zhou, "Effects of magnetic history on the levitation characteristics in a superconducting levitation system," *Physica C: Superconductivity,* vol. 468, no. 14, pp. 1013-1016, 2008.

[24] W. M. Yang and e. al., "Identification of the effect of grain size on levitation force of well-textured YBCO bulk superconductors," *Cryogenics,* vol. 42, no. 10, pp. 589-592, 2002.

[25] W. M. Yang, "Effect of perimeters of induced shielding current loops on levitation force in melt grown single-domain YBa2Cu3O7x bulk," *Applied Physics Letters,* vol. 79, no. 13, pp. 2043-2045, 2001.

[26] P. B. Landecker, D. D. Villani and K. W. Yung, "An Analytic Solution for the Torque between Two Magnetic Dipoles," *Physical Separation in Science and Engineering,* vol. 10, no. 1, pp. 29-33, 1999.

[27] K. W. Yung, P. B. Landecker and D. D. Villani, "An analytic solution for the force between two magnetic dipoles," *Physical Separation in Science and Engineering,* vol. 9, no. 1, pp. 39-52, 1998.

[28] C. H. Chiang and e. al., "Levitation force measurement at different temperatures for YBCO superconductor," *Journal of Low Temperature Physics,* vol. 131, no. 3, pp. 743-746, 2003.

[29] H. Jiang and e. al., "The magnetic levitation performance of YBaCuO bulk at different temperture," *Physic C: Superconductivity,* vol. 378, pp. 869-872, 2002.

[30] J. Halbritter, "Granular superconductors and their

intrinsic and extrinsic surface impedance," *Journal of Superconductivity,* vol. 8, no. 6, pp. 691-703, 1995.

[31] R. Liang, P. Dosanjh, D. A. Bonn, W. N. Hardy and A. J. Berlinsky, "Lower critical fields in an ellipsoid-shaped YBa2Cu3O6.95 single crystal," *Physical Review B,* vol. 50, no. 6, pp. 4212-4216, 1994.

[32] P. Chaddah, "Critical current densities in superconducting materials," *Sadhana,* vol. 28, no. 1-2, pp. 273-282, 2003.

[33] W. M. Yang and e. al., "The grain-alignment and its effect on the levitation force of melt processed YBCO single-domained bulk superconductors," *Physica C: Superconductivity,* vol. 307, no. 3, pp. 271-276, 1998.

[34] W. M. Yang and e. al., "The effect of different field cooling processes on the levitation force and attractive force of single-domain YBa2Cu3O7- x bulk.," *Superconductor Science and Technology ,* vol. 15, no. 10, p. 1410, 2002.

[35] W. M. Yang and e. al., "The effect of the grain alignment on the levitation force in single domain YBa2Cu3Oy bulk superconductors," *Physica C: Superconductivity,* vol. 319, no. 3, pp. 164-168, 1999.

[36] B. R. Weinberger, L. Lynds and J. R. Hull, "Magnetic bearings using high-temperature superconductors: some practical considerations," *Superconductor Science and Technology ,* vol. 3, no. 7, p. 381, 1990.

[37] L. Jones, "The dynamics and control of flux-pinned spacecraft systems: theory and experiment," Cornell University, Ithaca, 2012.

[38] W. C. Chan, C. Y. Wang and J. J. Lee, "Grain size effect on magnetic levitation of YBCO superconducting samples," *Physic C: Superconductivity,* vol. 282, pp. 1455-1456, 1997.

[39] M. K. Alqadi and e. al., "Interaction between a point magnetic dipole and a high-temperature superconducting sphere," *Physica B: Condensed Matter,* vol. 404, no. 12, pp. 1781-1784, 2009.

[40] Z. Ren and e. al., "Influence of shape and thickness on the levitation force of YBaCuO bulk HTS over a NdFeB guideway," *Physica C: Superconductivity,* vol. 384, no. 1, pp. 159-162, 2003.

[41] W. M. Yang and e. al., "The effect of magnet configurations on the levitation force of melt processed YBCO bulk superconductors," *Physica C: Superconductivity,* vol. 354, no. 1, pp. 5-12, 2001.

[42] CAN superconductors, "YBCO Levitation Bulk," [Online]. Available: http://www.can-superconductors.com/levitation-bulk.html. [Accessed 2017].

BIOGRAPHY

Frances Zhu *earned her B.S. in Mechanical and Aerospace Engineering from Cornell University, Ithaca in 2014 and is currently pursuing a Ph.D. in Aerospace Engineering at Cornell. Since 2014, she has been a Research Assistant with the Space Systems Design Studio, specializing in dynamics, systems, and controls engineering. Her research interests include flux pinned interface applications, spacecraft system architectures, robot dynamics, estimation, and controls. Ms. Zhu is a NASA Space Technology Research Fellow.*

Laura Jones-Wilson earned her Bachelor of Science in aerospace engineering with a minor in mathematics in 2007. Laura graduated in the summer of 2012 with her Ph.D. in Aerospace Engineering, with a concentration in Dynamics and Controls and a minor in Astronomy. She was awarded both the National Science Foundation (NSF) Graduate and the National Defense Science and Engineering Graduate (NDSEG) Fellowship. Presently, Dr. Jones-Wilson is a Guidance and Control Systems Engineer at NASA Jet Propulsion Laboratory.

Mason A. Peck *earned a B.S. in Aerospace Engineering from the University of Texas at Austin. He worked at Bell Helicopter from 1993 to 1994 on structural dynamics. From 1994 to 2001 he was an attitude dynamics specialist and systems engineer at Hughes Space and Communications (now Boeing Satellite Systems). During his years at Boeing he served as attitude dynamics lead in the Boeing mission control center, participating in real-time spacecraft operations and helping to resolve spacecraft performance anomalies. He earned his M.S. and Ph.D. at UCLA as a Howard Hughes Fellow from 1998 to 2001. In 2001 he joined Honeywell Defense and Space Systems , and in 2003 was named Principal Fellow. He has been issued several patents. In July of 2004, he joined the faculty at Cornell University, where he teaches courses in dynamics and control and in the mechanical and aerospace engineering program. He was promoted to Associate Professor in fall 2010. In 2012, he was appointed as NASA's Chief Technologist*